scientific reports

Check for updates

OPEN

Temperature-dependent optical and vibrational properties of $PtSe_2$ thin films

Desman P. Gulo[1], Han Yeh[2], Wen-Hao Chang[2] & Hsiang-Lin Liu[1]✉

$PtSe_2$ has received substantial research attention because of its intriguing physical properties and potential practical applications. In this paper, we investigated the optical properties of bilayer and multilayer $PtSe_2$ thin films through spectroscopic ellipsometry over a spectral range of 0.73–6.42 eV and at temperatures between 4.5 and 500 K. At room temperature, the spectra of refractive index exhibited several anomalous dispersion features below 1000 nm and approached a constant value in the near-infrared frequency range. The thermo-optic coefficients of bilayer and multilayer $PtSe_2$ thin films were $(4.31 \pm 0.04) \times 10^{-4}$/K and $(-9.20 \pm 0.03) \times 10^{-4}$/K at a wavelength of 1200 nm. Analysis of the optical absorption spectrum at room temperature confirmed that bilayer $PtSe_2$ thin films had an indirect band gap of approximately 0.75 ± 0.01 eV, whereas multilayer $PtSe_2$ thin films exhibited semimetal behavior. The band gap of bilayer $PtSe_2$ thin films increased to 0.83 ± 0.01 eV at 4.5 K because of the suppression of electron–phonon interactions. Furthermore, the frequency shifts of Raman-active E_g and A_{1g} phonon modes of both thin films in the temperature range between 10 and 500 K accorded with the predictions of the anharmonic model. These results provide basic information for the technological development of $PtSe_2$-based optoelectronic and photonic devices at various temperatures.

Two-dimensional transition-metal dichalcogenides (TMDs) have attracted considerable attention because of their novel physical properties in the reduced dimension and potential practical applications[1–5]. TMDs (common formula MX_2 [M = Mo, W; X = S, Se]) possess substantial band gap energies (approximately 1.0 to 2.0 eV) because of their quantum confinement effect and weak van der Waals forces[3,6–10]. Subsequent studies[11–13] have revealed that these characterizations can be altered simply by tuning their thickness. Furthermore, indirect to direct band gap transitions occur when the thickness is reduced to a monolayer. Additionally, TMDs exhibit high carrier mobility and high quantum efficiency of photoluminescence yield[12,14,15]. These superior properties make TMDs very attractive materials for use in optoelectronics[16], photovoltaic[17], and field-effect transistors[18].

$PtSe_2$ has received much research interest as an emerging TMDs material[19]. It exhibits unique thickness-dependent type-II Dirac semimetal to semiconducting transition[20,21]. Moreover, $PtSe_2$ exhibits strong interlayer coupling and excellent carrier mobility[22]. It is a promising material for use in next-generation sensors, optoelectronics, and ultrafast photonic devices[23–25]. Circular polarization calculations have revealed that single-layer $PtSe_2$ exhibits strong circular dichroism polarization along the M–K direction and near the Γ point. Thus, $PtSe_2$ is an excellent candidate for valleytronic devices[26]. In light of the many potential applications of $PtSe_2$, a comprehensive study of optical properties for $PtSe_2$ is essential. The temperature-dependent optical constants of $PtSe_2$ are critical references for determining the effects of self-heating on a device. O'Brien et al.[27] studied the Raman scattering spectra of direct-selenization grown $PtSe_2$ thin films as a function of film thickness, laser wavelength, and laser polarization. They found that the positions of phonon modes of $PtSe_2$ thin films exhibited a redshift with increase in the thickness from 0.5 to 5.0 nm. This phenomenon was attributed to domination of stacking-induced structural changes and Columbic interaction effects when the number of layers of the $PtSe_2$ thin films was increased. Yu et al.[28] reported that $PtSe_2$ thin films possess variable band gaps in the mid-infrared frequency region. They showed that monolayer $PtSe_2$ is suitable for use in visible and near-infrared photodetectors. Thus, bilayer $PtSe_2$ thin films are compatible with mid-infrared photodetectors and are an excellent candidate for photoelectronic devices. Xie et al.[29] investigated the room-temperature optical constants of $PtSe_2$ for different thicknesses through spectroscopic ellipsometry. They found that the values of refractive index and extinction coefficient exhibited a strong dependence on thickness.

[1]Department of Physics, National Taiwan Normal University, Taipei 11677, Taiwan. [2]Department of Electrophysics, National Chiao Tung University, Hsinchu 30010, Taiwan. ✉email: hliu@ntnu.edu.tw

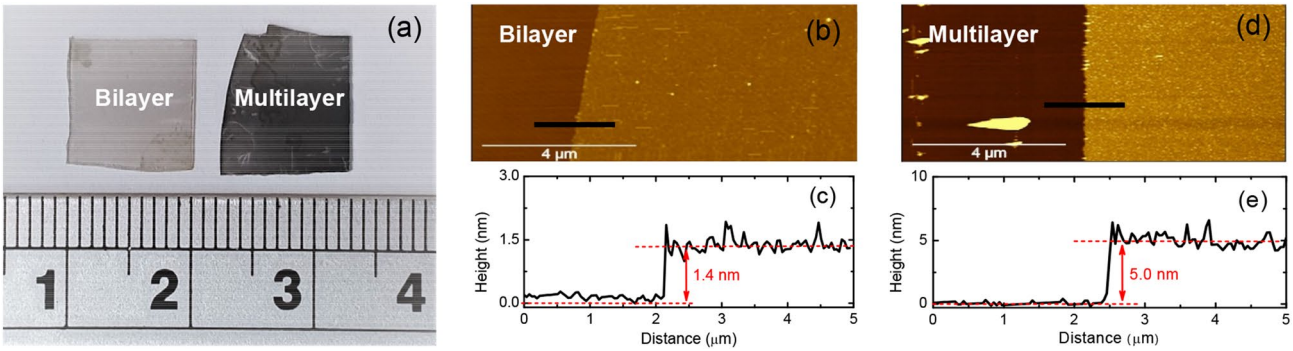

Figure 1. (**a**) Optical microscopic images of two $PtSe_2$ thin films. (**b**–**e**) Atomic force microscopic images and corresponding height profiles of two $PtSe_2$ thin films.

Layer type	Bilayer	Multilayer
Sapphire substrate (mm)	1	1
Film (nm)	1.45 ± 0.3	5.10 ± 0.6
Surface roughness (nm)	0.10 ± 0.02	0.25 ± 0.03

Table 1. Parameters of the stacked layer model fit for bilayer and multilayer $PtSe_2$ thin films.

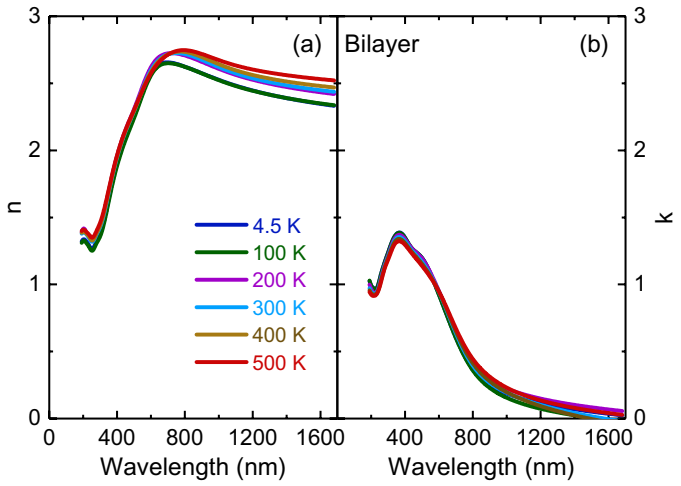

Figure 2. Temperature-dependent (**a**) refractive index and (**b**) extinction coefficient of bilayer $PtSe_2$ thin film.

Most optical measurements of $PtSe_2$ thin films have been limited to room temperature[27–29]. The temperature-dependent optical properties of $PtSe_2$ thin films have not been reported. In this paper, we characterized the optical constants of $PtSe_2$ thin films over a wide range of photon energy (from 0.73 to 6.42 eV) and temperature (between 4.5 and 500 K) through spectroscopic ellipsometry. We found that bilayer $PtSe_2$ thin films exhibited an indirect band gap and that multilayer $PtSe_2$ thin films exhibited semimetal behavior at 300 K. Furthermore, the band gap of bilayer $PtSe_2$ thin films increased from 0.71 ± 0.01 to 0.83 ± 0.01 eV when temperature decreased from 500 to 4.5 K. Multilayer $PtSe_2$ thin films exhibited a band gap of approximately 0.04 ± 0.004 eV at 500 K. Additionally, we investigated the temperature-dependent Raman scattering spectra of $PtSe_2$ thin films from 10 to 500 K. The temperature dependence of E_g and A_{1g} phonon modes was attributed to the anharmonic contributions to the interatomic potential energy, mediated by phonon–phonon interactions. These findings are highly promising for further development of $PtSe_2$ thin films in optoelectronic and photonic applications at various temperatures.

Experiment

Bilayer and multilayer $PtSe_2$ thin films were grown on sapphire substrates by using chemical vapor deposition method. Platinum (II) chloride ($PtCl_2$) and selenium (Se) were used as precursors. Both $PtSe_2$ samples with an area of approximately 1 cm^2 were formed at a temperature of 400 °C. The growth time ranged from 10 to 20 min for bilayer and multilayer thin films, respectively. The samples were prepared according to the method described in[21]. Figure 1 depicts the optical microscopic and atomic force microscopic images, and corresponding height

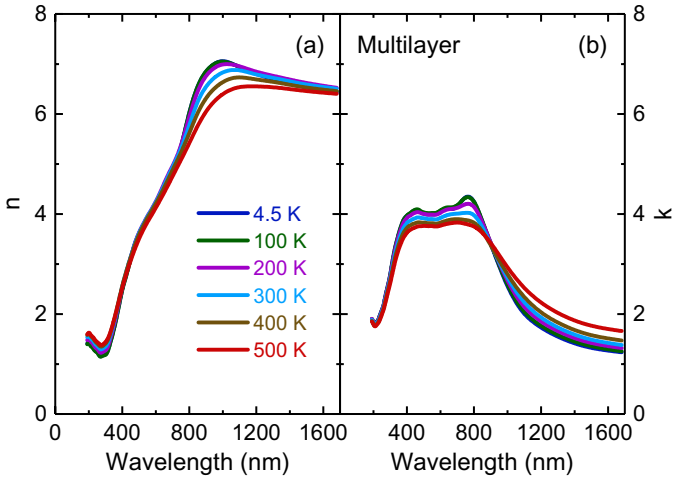

Figure 3. Temperature-dependent (**a**) refractive index and (**b**) extinction coefficient of multilayer $PtSe_2$ thin film.

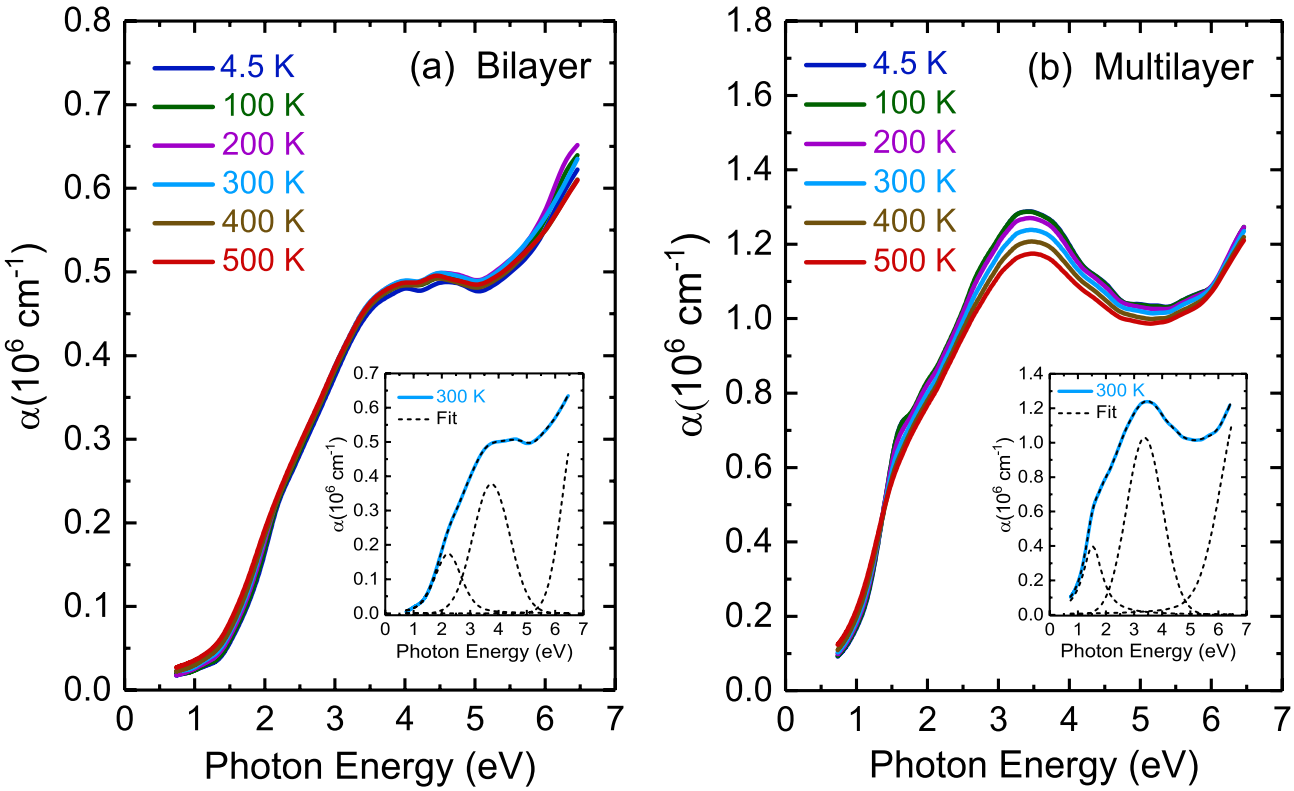

Figure 4. Temperature-dependent optical absorption spectra of (**a**) bilayer and (**b**) multilayer $PtSe_2$ thin films. The inset illustrates the best fit using the Lorentz-Gaussian function at 300 K.

profiles of two thin films. The thickness of these two thin films was approximately 1.4 and 5.0 nm, respectively, thus corresponding to two and seven $PtSe_2$ layers. Both thin films were also verified through transmission electron microscopy to be high-quality samples[30].

Room-temperature spectroscopic ellipsometry spectra were recorded under incident angles of 60°, 65°, 70°, and 75° and over a spectral range of 0.73 to 6.42 eV by using an ellipsometer (J. A. Woollam Co. M-2000U). For temperature-dependent measurements between 4.5 and 500 K, the samples were placed in a Janis ST-400 ultrahigh-vacuum continuous-flow helium cryostat[31,32]. The optical constants were obtained through spectroscopic ellipsometry using the stacked layer model (sapphire substrate/thin film/surface roughness/air ambient structure)[32]. The parameters of the model used to fit the raw ellipsometry data are listed in Table 1. The values of the mean square error are 1.07 and 1.40 for bilayer and multilayer $PtSe_2$ thin films. The independently measured

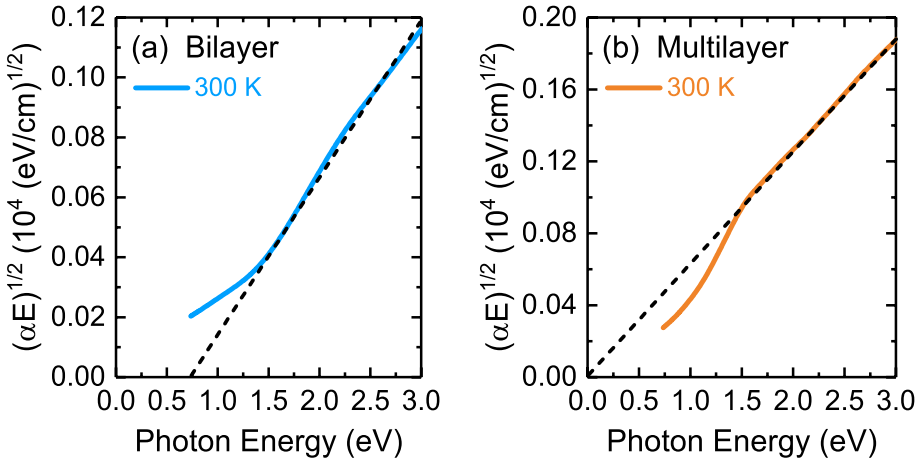

Figure 5. The plot of $(\alpha \cdot E)^{1/2}$ vs. photon energy enables the extraction of indirect band gap of (**a**) bilayer and (**b**) multilayer $PtSe_2$ thin films at 300 K.

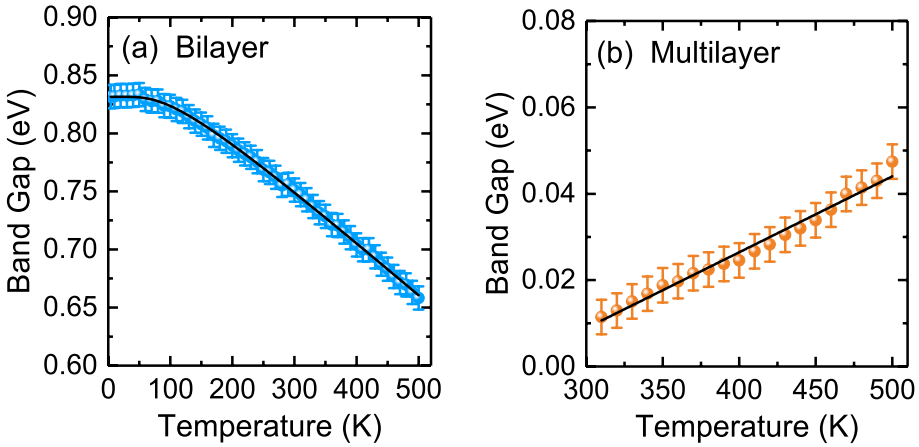

Figure 6. (**a**) Temperature-dependent indirect band gap of (**a**) bilayer and (**b**) multilayer $PtSe_2$ thin films. The thin solid lines indicate the results of the fitting using (**a**) the Bose–Einstein model and (**b**) the linear fit model.

experimental data at different incident angles and modeled curves exhibited good agreement (see Supplementary Figs. 1 and 2).

Room-temperature micro-Raman scattering measurements were performed using a backscattering geometry with a laser excitation wavelength of 532 nm[31]. The linear polarized light was focused to a 3-μm-diameter spot on the sample surface. Subsequently, a SENTERRA spectrometer collected and dispersed the scattered light with a 1024-pixel-wide charge-coupled detector. The spectral resolution achieved using these instruments was generally less than 0.5 cm^{-1}. To avoid heating effects, the laser power was set to less than 0.5 mW. The sapphire substrate exhibited high thermal conductivity and evacuated heating well[33]. The samples were mounted in a continuous-flow helium cryostat and LINKAM heating stage, which enabled measurements in the temperature range of 10–500 K[31].

Results and discussion

Figures 2 and 3 illustrate the temperature-dependent optical constant spectra of bilayer and multilayer $PtSe_2$ thin films recorded in a wavelength range of 193 to 1700 nm obtained through spectroscopic ellipsometry analysis. The spectra were almost identical by rotating the sample's azimuthal orientation of 45° and 90° shown in the Supplementary Figs. 3 and 4, indicating the in-plane isotropic optical properties of $PtSe_2$ thin films. For both thin films, the room-temperature refractive index increased substantially with an increase in the wavelength in the spectral range from 193 to 700 nm for bilayer and from 193 to 1100 nm for multilayer thin films. It then approached one maximum, which corresponded with the anomalous dispersion regime[34] and finally decreased with the wavelength until the wavelength reached 1700 nm. With an increase in layer thickness, the value of refractive index increased. This phenomenon is consistent with previous reports of thickness-dependent optical constants[29]. Notably, multilayer $PtSe_2$ thin film exhibited large refractive index values (approximately 6.88 at a wavelength of 1070 nm). Bilayer $PtSe_2$ thin film exhibited a maximum refractive index of approximately 2.72

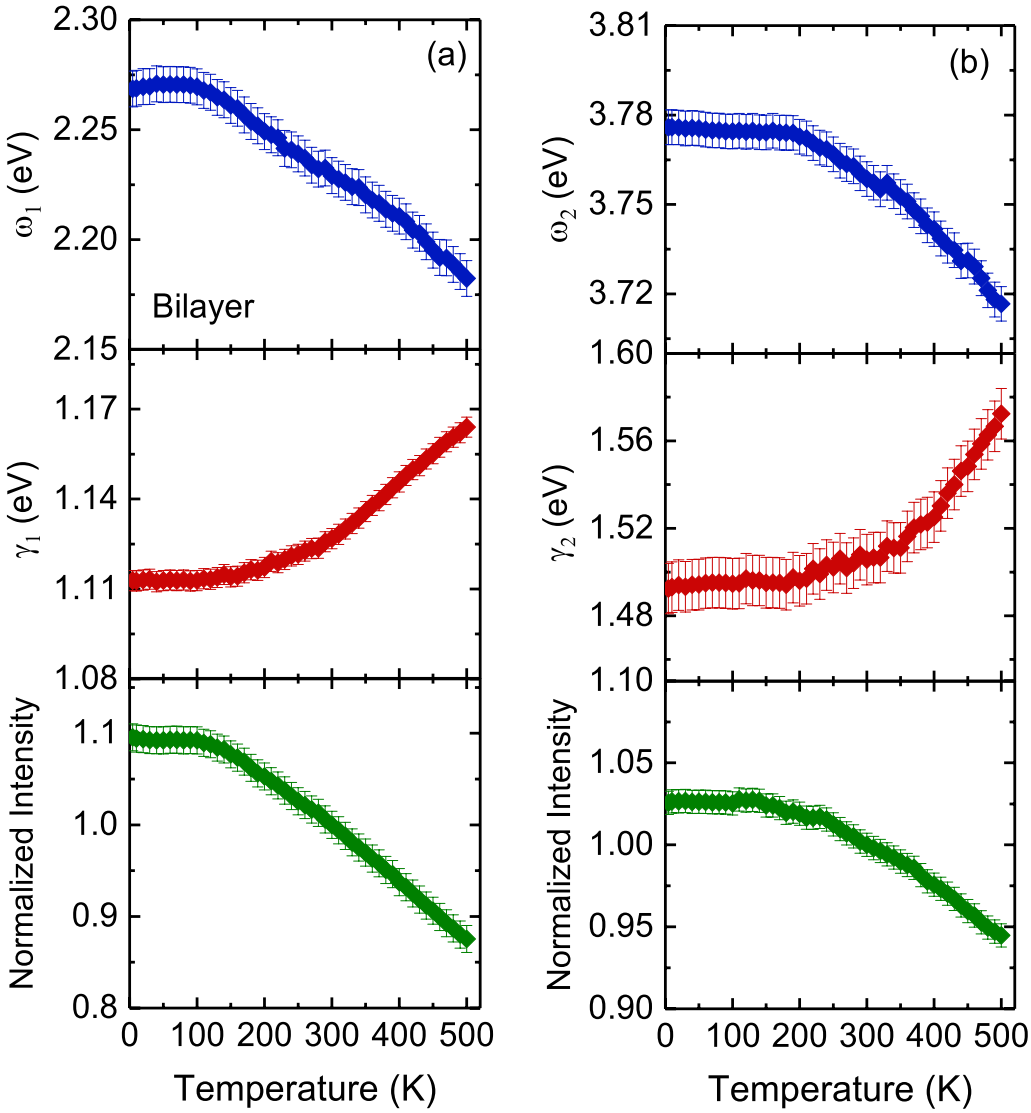

Figure 7. Temperature dependence of the peak energy, damping, and normalized intensity of (**a**) 2.22- and (**b**) 3.75-eV optical absorptions for bilayer $PtSe_2$ thin film.

at a wavelength of 720 nm. The characteristics of high refractive indices of bilayer and multilayer $PtSe_2$ thin films indicated a large scattering cross-section inside the crystal[35]. Thus, these effects are highly favorable for light trapping in photonic[36] and optoelectronic[37] devices in the visible to near-infrared frequency range. With a decrease in temperature, the refractive index of bilayer $PtSe_2$ thin film decreased in the near-infrared region. This behavior is ascribed to the decreased electron–phonon interaction with a decrease in temperature, as observed for other semiconducting TMDs, such as monolayer MoS_2, $MoSe_2$, WS_2, and WSe_2[32]. By contrast, this trend was reversed for multilayer $PtSe_2$ thin film, which could be associated with the enhanced electron–phonon interaction. The thermo-optic coefficients ($\partial n/\partial T$) for bilayer and multilayer $PtSe_2$ thin films were $(4.31 \pm 0.04) \times 10^{-4}$/K and $(-9.20 \pm 0.03) \times 10^{-4}$/K, respectively, at a wavelength of 1200 nm. Bilayer $PtSe_2$ thin film exhibited a positive thermo-optic coefficient value, similar to the coefficient of other semiconducting materials such as silicon[38]. By contrast, multilayer $PtSe_2$ thin film had a negative value of thermo-optic coefficient that was similar to the coefficient of TiO_2[39]. The negative thermo-optic coefficient observed in multilayer $PtSe_2$ may arise from the enhanced electron–phonon interaction at low temperatures because of its semimetallic properties. The extinction coefficient spectra (Figs. 2 and 3) of two thin films were featureless above 1000 nm, but exhibited several absorption peaks below 1000 nm. These absorptions exhibited a blueshift trend with a decrease in temperature. A detailed analysis of temperature-dependent optical absorption is provided later.

Figure 4 presents the temperature-dependent optical absorption coefficient spectra of two thin films. The absorption spectra were fitted using the Lorentzian-Gaussian function, as illustrated by the dashed lines in the inset of Fig. 4. Bilayer $PtSe_2$ thin film exhibited two optical absorption bands at approximately 2.22 and 3.75 eV. Multilayer $PtSe_2$ thin film revealed two optical absorption bands at approximately 1.51 and 3.39 eV. In accordance with previous reports[20,40], all absorption peaks for two thin films were assigned to charge-transfer excitations

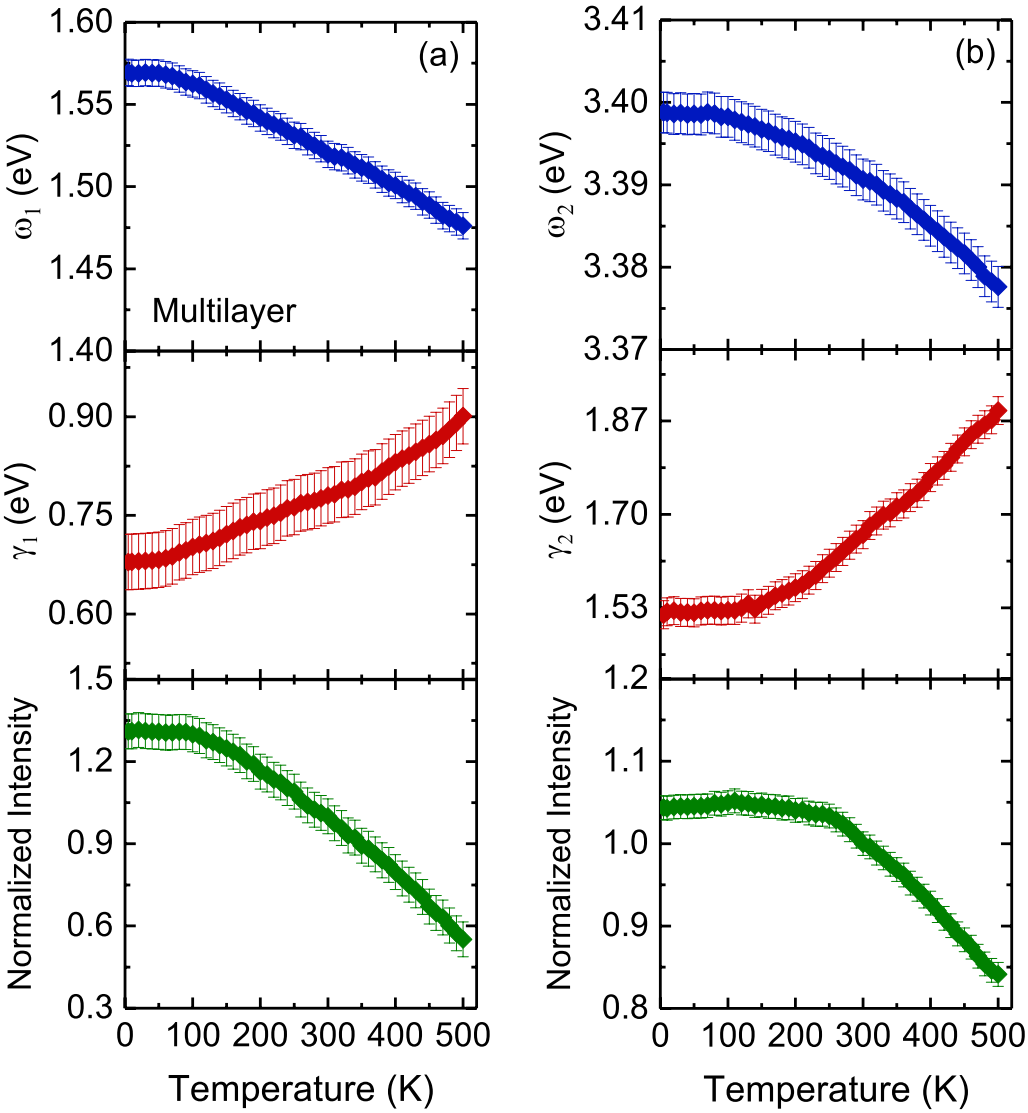

Figure 8. Temperature dependence of the peak energy, damping, and normalized intensity of (**a**) 1.51- and (**b**) 3.39-eV optical absorptions for multilayer $PtSe_2$ thin film.

between the hybridization of Pt 5*d* and Se 4*p* states at the valence and conduction band edges. Moreover, the first-principles calculations[20] predicted that the rapid decrease in band energy of conduction band states and increase in valence band states lead to metallization starting from trilayer $PtSe_2$ thin film. As a result, two absorption bands observed in multilayer $PtSe_2$ thin film exhibited a redshift as compared to those of bilayer $PtSe_2$ thin film. The band gap energy of bilayer and multilayer $PtSe_2$ thin films is depicted Fig. 5. The optical absorption coefficient, which includes contributions from both direct and indirect band gap transitions, was analyzed using the following expression[41]:

$$\alpha(E) = \frac{A}{E}\left(\mathrm{E} - E_{g,dir}\right)^{0.5} + \frac{B}{E}\left(E - E_{g,ind} \mp E_{ph}\right)^2 \quad (1)$$

where $E_{g,dir}$ and $E_{g,ind}$ are the magnitudes of direct and indirect band gaps, respectively; E_{ph} is the emitted (absorbed) phonon energy, and A and B are constants. This model, which assumes a simple band shape, enables extraction of the direct band gap when $(\alpha \cdot E)^2$ is plotted as a function of photon energy and extraction of indirect band gap when $(\alpha \cdot E)^{1/2}$ is plotted as a function of photon energy. Figure 5 presents an indirect band gap of approximately 0.75 ± 0.01 eV at 300 K for bilayer $PtSe_2$ thin film, whereas multilayer $PtSe_2$ thin film exhibited semimetal behavior from 300 to 4.5 K (see Supplementary Fig. 5). Plotting $(\alpha \cdot E)^2$ as a function of photon energy for both thin films led to a negative value for the band gap. The results of our band gap analysis of bilayer $PtSe_2$ thin film were consistent with those of other experimental studies[29,41,42]. However, the results for multilayer $PtSe_2$ thin film differed from those of other reports of semiconducting behavior in films of a similar thickness[29,42,43]. One possibility that could account for these differences is due to different quality of thin films.

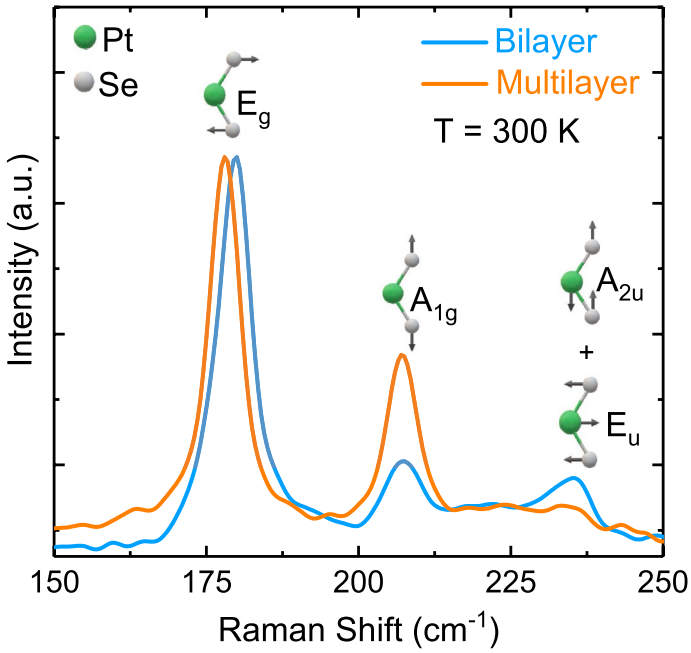

Figure 9. Raman scattering spectra of $PtSe_2$ thin films at room temperature. The inset illustrates vibrational modes of both $PtSe_2$ thin films [50].

Layer type	ω_1 /E_g (cm^{-1})	ω_2/A_{1g} (cm^{-1})	ω_3/LO (cm^{-1})
Bilayer	179	207	235
Multilayer	178	207	232

Table 2. Raman phonon modes observed at room temperature for bilayer and multilayer $PtSe_2$ thin films with their corresponding assignments.

Figure 6 displays the temperature dependence of the band gap of bilayer and multilayer $PtSe_2$ thin films. The band gap of bilayer $PtSe_2$ thin film increased with a decrease in temperature. The observed blueshift value of the band gap energy with decreasing temperature in semiconductors can be described using the Bose–Einstein model as follows[44]:

$$E_g(T) = E_g(0) - \frac{2a_B}{\exp\left(\frac{\Theta_B}{T}\right) - 1}, \quad (2)$$

where E_g (0) represents the band gap at 0 K, a_B is the strength of the electron–phonon interactions, and Θ_B is the average phonon temperature. Our fitting results indicated that the band gap energy toward 0 K was approximately 0.83 ± 0.01 eV. The strength of the electron–phonon interactions a_B and the average phonon temperature Θ_B were 66 meV and 288 K, respectively. These values are comparable to those obtained for other semiconducting materials such as ZnS[45] and ZnSe[46]. In contrast to bilayer $PtSe_2$ thin film, multilayer $PtSe_2$ thin film revealed a band gap energy that steadily increased with an increase in temperature from 310 to 500 K. This could induce semimetal to semiconducting transition and may be due to both the electron–phonon interaction and thermal expansion of the lattice[47]. The linearly fitted result indicated that the temperature coefficient was 1.75×10^{-4} eV/K. This value is lower than those of other TMDs such as ReS_2[48]. Figures 7 and 8 illustrate the peak energy, damping, and normalized intensity of 2.22- and 3.75-eV optical transitions for bilayer $PtSe_2$ thin film and 1.51- and 3.39-eV optical transitions for multilayer $PtSe_2$ thin film as a function of temperature. The peak positions of all absorption bands shifted to higher photon energies, resonance damping narrowed, and normalized intensity increased with a decrease in temperature.

Figure 9 depicts the room-temperature Raman scattering spectra of bilayer and multilayer $PtSe_2$ thin films. The spectra comprised three Raman phonon modes. We fitted these phonon peaks using a standard Lorentzian profile. The phonon frequency and assignment are summarized in Table 2. According to the results of factor group analysis, $PtSe_2$ had a 1 *T*-type hexagonal crystal structure (*P-3m1*) with one formula unit per primitive cell[27]. The irreducible representation of the phonon modes at the center of the Brillouin zone is expressed by $\Gamma = A_{1g} + E_g + 2A_{2u} + 2E_u$[27]. These modes are classified as Raman active ($A_{1g} + E_g$), infrared active ($2A_{2u}$), and Raman and infrared active ($2E_u$). We observed two main peaks at approximately 179 and 207 cm^{-1} in bilayer $PtSe_2$ thin

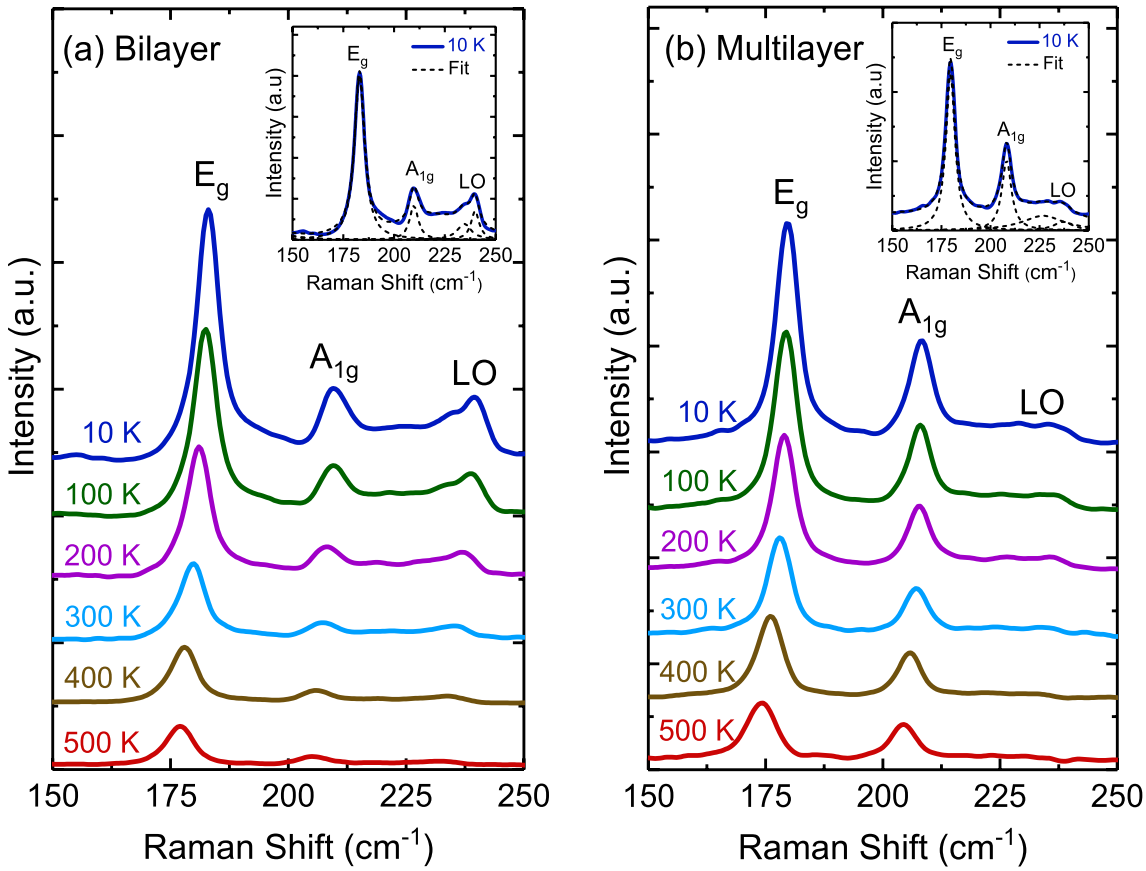

Figure 10. Temperature-dependent Raman scattering spectra of (**a**) bilayer and (**b**) multilayer $PtSe_2$ thin films. The inset displays Raman scattering spectrum with Lorentzian oscillators of bilayer and multilayer $PtSe_2$ thin films at 10 K.

film, which were associated with the zone center and first-order one-phonon emission for in-plane and out-of-plane with E_g and A_{1g} symmetries, respectively. The peak frequencies (179 and 207 cm^{-1}) reproduced previous Raman scattering measurements, indicating a bilayer signature[27]. Additionally, we observed one less-predominant peak at approximately 235 cm^{-1}, which corresponded to the longitudinal optical (LO) mode in bilayer $PtSe_2$ thin film. This mode is mainly separated into two vibrations that correspond to first-order two-phonon emissions for out-plane (A_{2u}) and in-plane (E_u) motions of Pt and Se atoms. Similar phonon modes have been observed in CdI_2 as the same structure with $PtSe_2$ thin films[49].

In the normalized condition of the intensity of the E_g mode, two phonon modes (E_g and LO) of $PtSe_2$ thin film shifted to lower frequency ranges (from 179 and 235 cm^{-1} [bilayer] to 178 and 232 cm^{-1} [multilayer], respectively) with an increase in the number of layers. Unlikely those two phonon modes, the frequency of the A_{1g} mode of bilayer $PtSe_2$ thin film was unchanged when the number of layers increased. This anomalous behavior is consistent with that of $PtSe_2$ thin film growth through molecular beam epitaxy[50]. Subsequently, we observed that the A_{1g} mode of multilayer $PtSe_2$ thin film exhibited higher intensity than that of bilayer $PtSe_2$ thin film because of stacking-induced structural changes and long-range Coulombic interlayer interactions[51]. The intensity of the LO mode decreased with an increase in thickness. This behavior could be associated with the enhanced interlayer coupling in multilayer $PtSe_2$ thin film[27].

Figure 10 displays the temperature dependence of the Raman scattering spectra of bilayer and multilayer $PtSe_2$ thin films. When the temperature decreased, the peak positions of all phonon modes shifted to higher frequencies, and their resonance linewidth decreased. The Raman scattering spectra exhibited sharp phonon modes at 10 K for both thin films. Four Lorentzian oscillators were used to represent the Raman scattering spectrum at 10 K (inset of Fig. 10), whereas the background was taken to be linear in these fits of the form $A\omega + B$, where A and B are adjustable parameters. Figures 11 and 12 illustrate the frequency, linewidth, and normalized intensity of phonon modes as functions of temperature. The phonon modes changed continuously from temperatures of 500 to 10 K. In a normal anharmonic solid, a decrease in temperature causes an increase in phonon frequency but a decrease in linewidth. Anharmonic interactions are relevant to higher-order terms of atomic vibrations that are beyond traditional harmonic terms. The temperature-dependent phonon frequency and linewidth can be expressed as follows[52]:

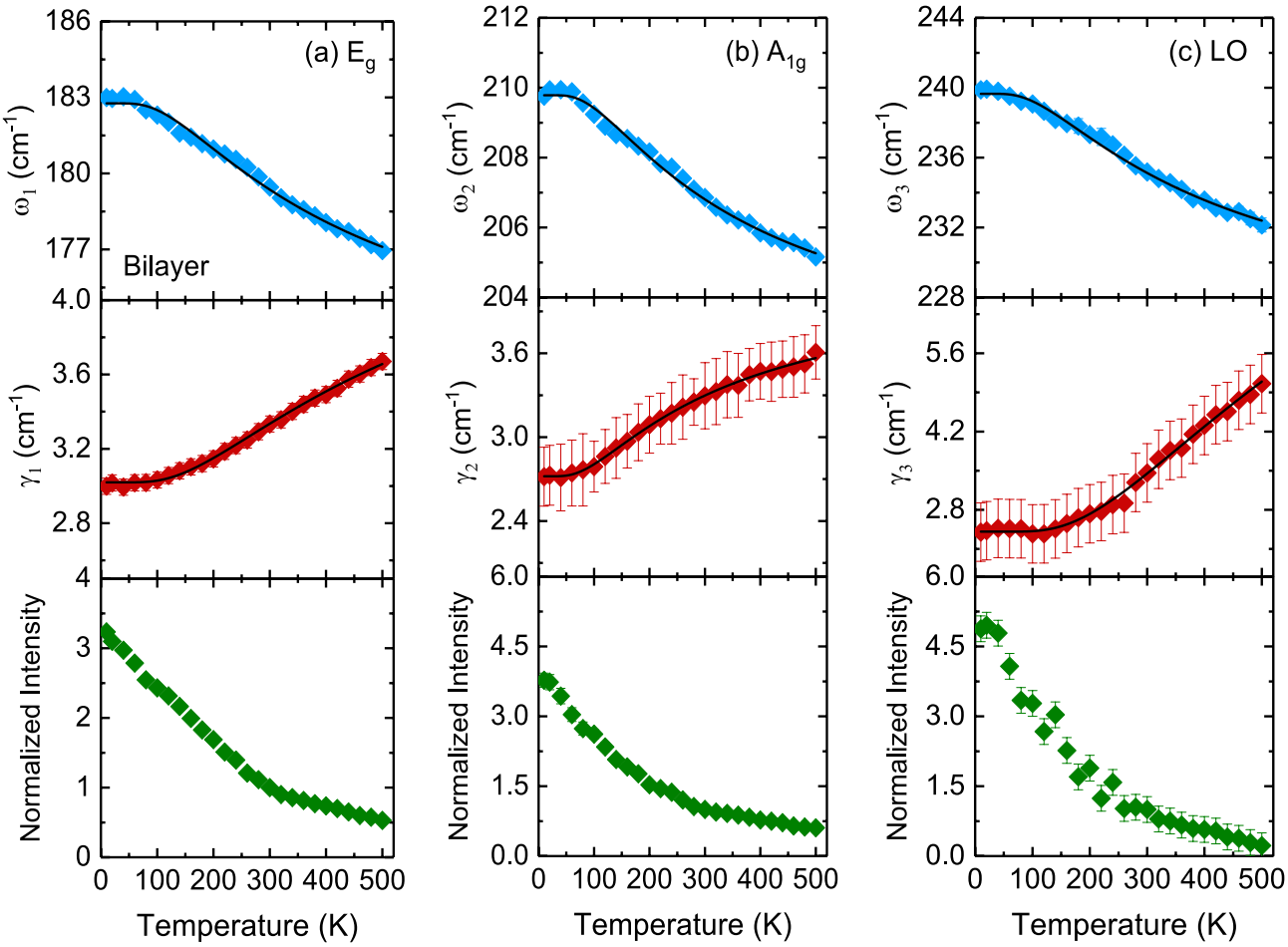

Figure 11. Temperature dependence of the frequency, linewidth, and normalized intensity of (**a**) E_g, (**b**) A_{1g}, and (**c**) LO modes for bilayer $PtSe_2$ thin film. The thin solid lines indicate the results of the fitting from the anharmonic model by using Eqs. (3) and (4).

$$\omega(T) = \omega_0 + A\left(1 + \frac{2}{exp\left(\frac{\Theta}{T}\right) - 1}\right) \tag{3}$$

$$\gamma(T) = \gamma_0 + B\left(1 + \frac{2}{exp\left(\frac{\Theta}{T}\right) - 1}\right) \tag{4}$$

where ω_0 is the intrinsic frequency of the optical phonon mode, γ_0 is linewidth broadening due to defects, A and B are anharmonic coefficients, and Θ is the Debye temperature. The values of the fitting parameters are summarized in Table 3.

Table 3 indicates that the high absolute A values of E_g and A_{1g} modes in bilayer and multilayer $PtSe_2$ thin films revealed a dominant anharmonic interaction between Pt and Se atoms. These large values are crucial for reducing lattice thermal conductivity[53]. The relatively small absolute B values of E_g and A_{1g} modes in bilayer and multilayer $PtSe_2$ thin films were associated with strong anharmonic phonon–phonon interactions. Thus, anharmonic phonon scattering with three-phonon process (Eqs. 3 and 4) is highly favorable for bilayer and multilayer $PtSe_2$ thin films. At a temperature of 10 K, as depicted in Fig. 10, the LO phonon mode of bilayer $PtSe_2$ thin film exhibited a peak position that split into two-phonon modes (A_{2u} and E_u) at approximately 235 and 239 cm^{-1}. By contrast, multilayer $PtSe_2$ thin film exhibited a broadening peak at approximately 236 cm^{-1}. Moreover, the A_{2u} and E_u phonon modes of bilayer $PtSe_2$ thin film exhibited a blueshift and an increase in intensity in temperature with a decrease in temperature.

Summary. The temperature-dependent optical properties of bilayer and multilayer $PtSe_2$ thin films were investigated through spectroscopic ellipsometry and Raman scattering spectroscopy. Large value of the refractive index (approximately 6.88) in the near-infrared frequency range was obtained for multilayer $PtSe_2$ thin film. The thermo-optic coefficients of bilayer and multilayer $PtSe_2$ thin films were $(4.31 \pm 0.04) \times 10^{-4}$/K and $(-9.20 \pm 0.03) \times 10^{-4}$/K at a wavelength of 1200 nm. The room-temperature optical absorption spectra revealed

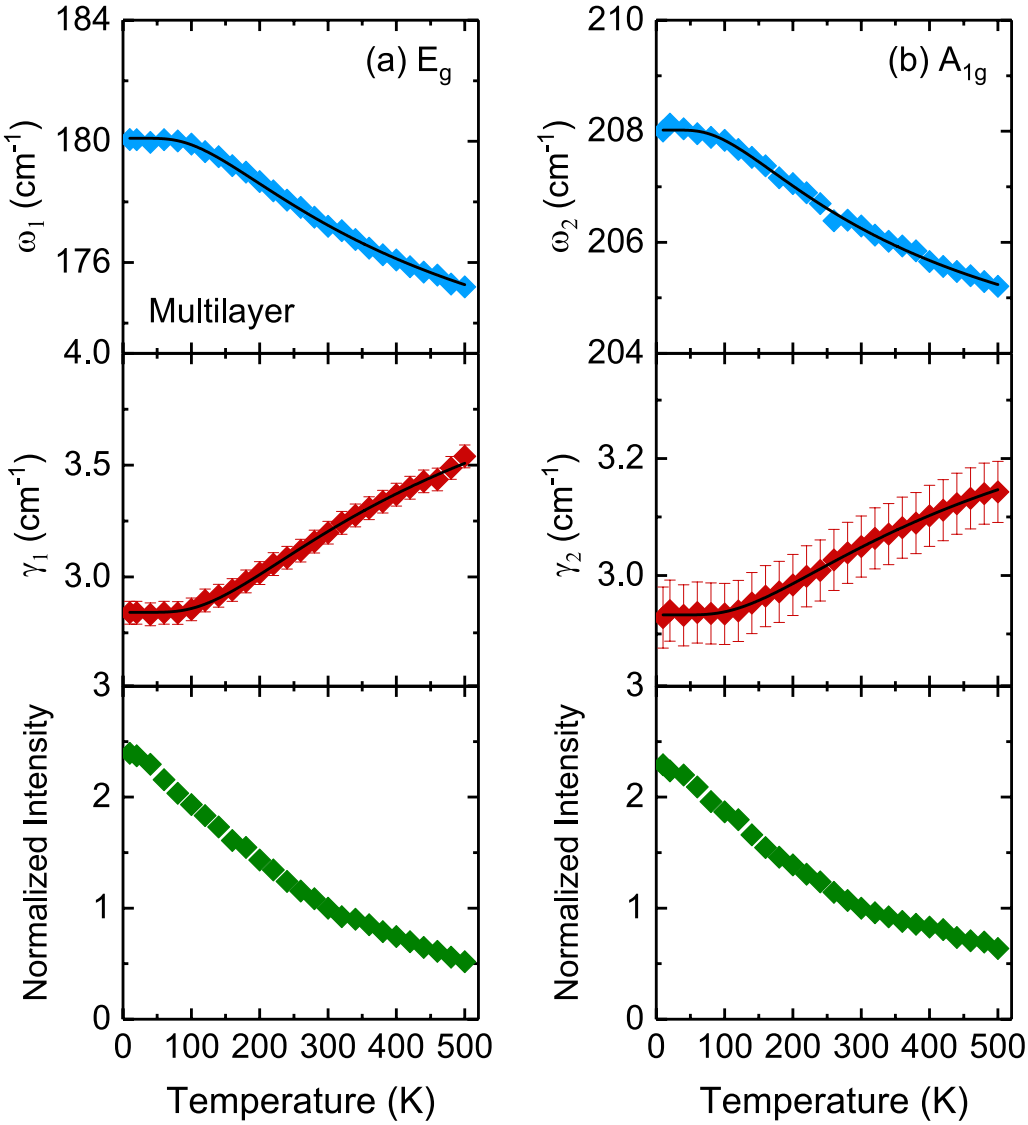

Figure 12. Temperature dependence of the frequency, linewidth, and normalized intensity of (**a**) E_g and (**b**) A_{1g} modes for multilayer $PtSe_2$ thin film. The thin solid lines indicate the results of the fitting from the anharmonic model by using Eqs. (3) and (4).

Layer type	Mode	ω_0 (cm^{-1})	γ_0 (cm^{-1})	A (cm^{-1})	B (cm^{-1})	Θ(K)
Bilayer	E_g	182.8	3.0	−6.1	0.9	382
	A_{1g}	209.8	2.6	−4.2	0.7	313
Multilayer	E_g	180.1	2.8	−5.2	0.8	390
	A_{1g}	208	2.9	−2.7	0.3	339

Table 3.. Parameter values obtained from fitting the temperature dependence of phonon frequencies and linewidths according to the anharmonic model using Eqs. (3) and (4).

that bilayer $PtSe_2$ thin film had an indirect band gap of approximately 0.75 ± 0.01 eV, whereas multilayer $PtSe_2$ thin film exhibited semimetal behavior. The band gap of bilayer $PtSe_2$ thin film increased to 0.83 ± 0.01 eV at 4.5 K. By contrast, multilayer $PtSe_2$ thin film exhibited a band gap energy of approximately 0.04 ± 0.004 eV at 500 K. Moreover, the temperature-dependent phonon frequency and linewidth of Raman-active E_g and A_{1g} modes of both thin films accorded with the predictions of the anharmonic model. These results provide fundamental information regarding $PtSe_2$-based devices for optoelectronic and photonic applications at various temperatures.

Data availability statement

The data that support the findings of this study are available from the corresponding author upon reasonable request.

Received: 15 August 2020; Accepted: 23 October 2020
Published online: 04 November 2020

References

1. Duan, X., Wang, C., Pan, A., Yu, R. & Duan, X. Two-dimensional transition metal dichalcogenides as atomically thin semiconductors: opportunities and challenges. *Chem. Soc. Rev.* **44**, 8859 (2015).
2. Manzeli, S., Ovchinnikov, D., Pasquier, D., Yazyev, O. V. & Kis, A. 2D transition metal dichalcogenides. *Nat. Rev. Mater.* **2**, 17033 (2017).
3. Roldán, R. *et al.* Electronic properties of single-layer and multilayer transition metal dichalcogenides MX_2 (M = Mo, W and X = S, Se). *Ann. Phys.* **526**, 347 (2014).
4. Jariwala, D., Sangwan, V. K., Lauhon, L. J., Marks, T. J. & Hersam, M. C. Emerging device applications for semiconducting two-dimensional transition metal dichalcogenides. *ACS Nano* **8**, 1102 (2014).
5. Kolobov, A. V. & Tominaga, J. *Two-Dimensional Transition-Metal Dichalcogenides* (Springer, New York, 2016).
6. Mak, K. F., Lee, C., Hone, J., Shan, J. & Heinz, T. F. Atomically thin MoS_2: a new direct-gap semiconductor. *Phys. Rev. Lett.* **105**, 136805 (2010).
7. Zhao, W. *et al.* Origin of indirect optical transitions in few-layer MoS_2, WS_2, and WSe_2. *Nano Lett.* **13**, 5627 (2013).
8. Liu, H. L., Shen, C. C., Su, S. H., Hsu, C. L., Li, M. Y. & Li, L. J. Optical properties of monolayer transition metal dichalcogenides probed by spectroscopic ellipsometry. *Appl. Phys. Lett.* **105**, (2014).
9. Li, J., Chen, X., Zhang, D. & Zhou, P. Van der Waals heterostructure based field effect transistor application. *Crystals* **8**, 8 (2017).
10. Sangwan, V. K. & Hersam, M. C. Electronic transport in two-dimensional materials. *Annu. Rev. Phys. Chem.* **69**, 299 (2018).
11. Nguyen, H. T. *et al.* Temperature dependence of optical properties of monolayer WS_2 by spectroscopic ellipsometry. *Appl. Surf. Sci.* **511**, 145503 (2020).
12. Choi, W. *et al.* Recent development of two-dimensional transition metal dichalcogenides and their applications. *Mater. Today* **20**, 116 (2017).
13. Chen, H.-Y., Palummo, M., Sangalli, D. & Bernardi, M. Theory and ab initio computation of the anisotropic light emission in monolayer transition metal dichalcogenides. *Nano Lett.* **18**, 3839 (2018).
14. Choi, B. K. *et al.* Temperature dependence of band gap in $MoSe_2$ grown by molecular beam epitaxy. *Nanoscale Res. Lett.* **12**, 492 (2017).
15. Huo, N. *et al.* High carrier mobility in monolayer CVD-grown MoS_2 through phonon suppression. *Nanoscale* **10**, 15071 (2018).
16. Wang, Q. H., Kalantar-Zadeh, K., Kis, A., Coleman, J. N. & Strano, M. S. Electronics and optoelectronics of two-dimensional transition metal dichalcogenides. *Nat. Nanotechnol.* **7**, 699 (2012).
17. Wu, K., Ma, H., Gao, Y., Hu, W. & Yang, J. Highly-efficient heterojunction solar cells based on two-dimensional tellurene and transition metal dichalcogenides. *J. Mater. Chem. A* **7**, 7430 (2019).
18. Rawat, B., Vinaya, M. M. & Paily, R. Transition metal dichalcogenide-based field-effect transistors for analog/mixed-signal applications. *IEEE Trans. Electron Devices* **66**, 2424 (2019).
19. Yang, Y., Jang, S. K., Choi, H., Xu, J. & Lee, S. Homogeneous platinum diselenide metal/semiconductor coplanar structure fabricated by selective thickness control. *Nanoscale* **11**, 21068 (2019).
20. Kandemir, A. *et al.* Structural, electronic and phononic properties of PtSe2: from monolayer to bulk. *Semicond. Sci. Technol.* **33**, 085002 (2018).
21. Shi, J. *et al.* Chemical vapor deposition grown large-scale atomically thin platinum diselenide with semimetal–semiconductor transition. *ACS Nano* **13**, 8442 (2019).
22. Zhao, Y. *et al.* High-electron-mobility and air-stable 2D layered $PtSe_2$ FETs. *Adv. Mater.* **29**, 1604230 (2017).
23. Yim, C. *et al.* High-performance hybrid electronic devices from layered $PtSe_2$ films grown at low temperature. *ACS Nano* **10**, 9550 (2016).
24. Zeng, L. *et al.* Ultrafast and sensitive photodetector based on a $PtSe_2$/silicon nanowire array heterojunction with a multiband spectral response from 200 to 1550 nm. *NPG Asia Mater.* **10**, 352 (2018).
25. Yuan, J. *et al.* Few-layer platinum diselenide as a new saturable absorber for ultrafast fiber lasers. *ACS Appl. Mater. Interfaces* **10**, 21534 (2018).
26. Wang, Y. *et al.* Monolayer $PtSe_2$, a new semiconducting transition-metal-dichalcogenide, epitaxially grown by direct selenization of Pt. *Nano Lett.* **15**, 4013 (2015).
27. O'Brien, M. *et al.* Raman characterization of platinum diselenide thin films. *2D Mater.* **3**, 021004 (2016).
28. Yu, X. *et al.* Atomically thin noble metal dichalcogenide: a broadband mid-infrared semiconductor. *Nat. Commun.* **9**, 1545 (2018).
29. Xie, J. *et al.* Optical properties of chemical vapor deposition-grown $PtSe_2$ characterized by spectroscopic ellipsometry. *2D Mater.* **6**, 035011 (2019).
30. Yeh, H., Wu, Y., Yeh, T., Li, C., Chou, Y., Li, M., Chou, Y., Luo, C. W., Li, L. & Chang, W. H. Scalable fabrication of $PtSe_2$ metal-semiconductor lateral junctions via local layer engineering (private communication).
31. Chen, H. W. *et al.* Spin-charge-lattice coupling in $YBaCuFeO_5$: Optical properties and first-principles calculations. *Sci. Rep.* **9**, 3223 (2019).
32. Liu, H. L. *et al.* Temperature-dependent optical constants of monolayer MoS_2, $MoSe_2$, WS_2, and WSe_2: spectroscopic ellipsometry and first-principles calculations. *Sci. Rep.* **10**, 15282 (2020).
33. Hashmi, S. *Reference Module in Materials Science and Materials Engineering* (Elsevier, Oxford, 2016).
34. Hecht, E. *Optics* (Addison Wesley, London, 2002).
35. Born, M. & Wolf, E. *Principles of Optics - 7th (Expanded) Edition* (Cambridge University Press, Cambridge, 1999).
36. Soref, R. The past, present, and future of silicon photonics. *IEEE J. Sel. Top. Quantum Electron.* **12**, 1678 (2006).
37. Ma, M. *et al.* Enhancement of photovoltaic cell response due to high-refractive-index encapsulants. *J. Appl. Phys.* **108**, 043102 (2010).
38. Komma, J., Schwarz, C., Hofmann, G., Heinert, D. & Nawrodt, R. Thermo-optic coefficient of silicon at 1550 nm and cryogenic temperatures. *Appl. Phys. Lett* **101**, 041905 (2012).
39. Wiechmann, S. & Müller, J. Thermo-optic properties of TiO_2, Ta_2O_5 and Al_2O_3 thin films for integrated optics on silicon. *Thin Solid Films* **517**, 6847 (2009).
40. Sajjad, M., Singh, N. & Schwingenschlögl, U. Strongly bound excitons in monolayer PtS_2 and $PtSe_2$. *Appl. Phys. Lett.* **112**, 043101 (2018).
41. Pankove, J. I. *Optical Proccesses in Semiconductors* (Springer, New York, 1971).

42. Zhao, X. *et al.* Thickness-dependent ultrafast nonlinear absorption properties of $PtSe_2$ films with both semiconducting and semimetallic phases. *Appl. Phys. Lett.* **115**, 263102 (2019).
43. Chen, X. *et al.* Direct observation of interlayer coherent acoustic phonon dynamics in bilayer and few-layer $PtSe_2$. *Photonics Res.* **7**, 1416 (2019).
44. O'Donnell, K. P. & Chen, X. Temperature dependence of semiconductor band gaps. *Appl. Phys. Lett.* **58**, 2924 (1991).
45. Pässler, R. *et al.* Temperature dependence of exciton peak energies in ZnS, ZnSe, and ZnTe epitaxial films. *J. Appl. Phys.* **86**, 4403 (1999).
46. Pejova, B., Abay, B. & Bineva, I. Temperature dependence of the band-gap energy and sub-band-gap absorption tails in strongly quantized ZnSe nanocrystals deposited as thin films. *J. Phys. Chem. C* **114**, 15280 (2010).
47. Gibbs, Z. M. *et al.* Temperature dependence band gap in PbX (X = S, Se, Te). *Appl. Phys. Lett.* **103**, 262109 (2013).
48. Zhao, K. *et al.* Temperature dependence of phonon modes, optical constants, and optical band gap in two-dimensional ReS_2 films. *J. Phys. Chem. C* **122**, 29464 (2018).
49. Cingolani, A., Ferrara, M., Lugarà, M. & Lévy, F. The Raman spectra of CdI_2. *Solid State Commun.* **50**, 911 (1984).
50. Yan, M. *et al.* High quality atomically thin $PtSe_2$ films grown by molecular beam epitaxy. *2D Mater.* **4**, 1 (2017).
51. Lee, C. *et al.* Anomalous lattice vibrations of single- and few-layer MoS_2. *ACS Nano* **4**, 2695 (2010).
52. Balkanski, M., Wallis, R. F. & Haro, E. Anharmonic effects in light scattering due to optical phonons in silicon. *Phys. Rev. B* **28**, 1928 (1983).
53. Chen, L.-C. *et al.* Phonon anharmonicity in thermoelectric palladium sulfide by Raman spectroscopy. *Appl. Phys. Lett.* **113**, 022105 (2018).

Acknowledgements

H.L.L. thanks financial support from the Ministry of Science and Technology of Republic of China under Grants No. MOST 109-2112-M-003-016. W.H.C. thanks financial support from the Ministry of Science and Technology of Republic of China under Grants No. 108-2119-M-009-011-MY3.

Author contributions

H.L.L. conceived the research and was responsible for the experimental design. D.P.G. conducted the experiments. H.Y. and W.H.C. were responsible for the sample preparation. D.P.G. and H.L.L. drafted the paper. All contributing authors have discussed the results and provided the comments regarding the manuscript.

Competing interests

The authors declare no competing interests.

Additional information

Supplementary information is available for this paper at https://doi.org/10.1038/s41598-020-76036-y.

Correspondence and requests for materials should be addressed to H.-L.L.

Reprints and permissions information is available at www.nature.com/reprints.

Publisher's note Springer Nature remains neutral with regard to jurisdictional claims in published maps and institutional affiliations.